Solar RRL

RESEARCH ARTICLE OPEN ACCESS

Benchmarking Inorganic Deposition Routes for Hybrid Two-Step Processed Perovskite Solar Cells: A Materials Perspective

Julian Petry[1,2] | Ronja Pappenberger[1,2] | Alexander Welle[3,4] | Tonghan Zhao[1] | Alexander Diercks[2] | Raphael Pesch[1,2] | Moritz Krause[2] | Paul Fassl[1,2] | Ulrich W. Paetzold[1,2]

[1]Institute of Microstructure Technology (IMT), Karlsruhe Institute of Technology (KIT), Eggenstein-Leopoldshafen, Germany | [2]Light Technology Institute (LTI), Karlsruhe Institute of Technology (KIT), Karlsruhe, Germany | [3]Institute of Functional Interfaces (IFG), Karlsruhe Institute of Technology (KIT), Eggenstein-Leopoldshafen, Germany | [4]Karlsruhe Nano Micro Facility (KNMFi), Karlsruhe Institute of Technology (KIT), Eggenstein-Leopoldshafen, Germany

Correspondence: Ronja Pappenberger (ronja.pappenberger@kit.edu) | Ulrich W. Paetzold (ulrich.paetzold@kit.edu)

Received: 2 September 2025 | **Revised:** 24 December 2025 | **Accepted:** 13 January 2026

Keywords: crystallinity | hybrid route | microstructure | perovskite solar cell | vapor deposition

ABSTRACT

As the perovskite solar cell (PSC) industry moves toward large-scale manufacturing, production processes must enable high-throughput fabrication and simple process integration. The hybrid two-step deposition route has emerged as a promising method for achieving conformal coatings on micron-scale textures, a critical feature for perovskite/silicon tandem photovoltaics. In this work, we present a fully sequential route, wherein the inorganic materials CsCl and PbI_2 are deposited separately, allowing for facile industrial implementation as compared to the commonly codeposited inorganic scaffold. Microstructural analysis reveals a change in preferred crystal orientation of the PbI_2 platelets with codeposition resulting in horizontal growth, whereas sequential deposition promotes vertical growth with a secondary tilted orientation. Elemental mapping of the final perovskite absorber shows homogeneous distribution of Cs, formamidinium, and I, while Pb and Cl largely retain their initial scaffold positions. PSCs fabricated via sequential deposition of the inorganic scaffold demonstrate improved process repeatability and reach an efficiency of 20.3%, ranking among the highest reported efficiencies for wide-bandgap hybrid two-step processed PSCs. These findings underscore the potential of fully sequential hybrid deposition as a viable route toward industrial PSC production.

1 | Introduction

Perovskite solar cells (PSCs) have demonstrated an unprecedented progress in achieved power conversion efficiency (PCE) over the past decade. Since their first report in 2009 with a PCE of 3.8%, single-junction (SJ) PSCs approach an efficiency of 27% today, positioning them as strong future competitor to established silicon (Si) photovoltaic technologies [1, 2]. In particular, inverted PSCs (*p*–*i*–*n* architecture) have attracted significant interest due to their compatibility with p-type Si bottom cells in monolithic tandem configuration. Perovskite/Si tandem solar cells (TSCs) have already surpassed the theoretical efficiency limit of SJ Si solar cells [3], achieving record efficiencies exceeding 34% [2], and are considered as promising candidates for next-generation, high-efficiency photovoltaic modules [4–9]—given that remaining stability challenges are resolved [10].

Commercial Si bottom cells typically feature random pyramidal textures (2–5 μm in height), exhibiting enhanced light-harvesting properties compared to planar or polished surfaces [11–16]. However, depositing uniform, high-quality perovskite layers on such textured surfaces remains challenging—a critical

---

Julian Petry and Ronja Pappenberger contributed equally to this study.

requirement for industrial-scale monolithic tandem integration [4]. Conventional solution-based methods struggle to provide conformal coating on micron-scale textures, often resulting in poor surface coverage and reduced device performance [17, 18]. Alternatively, vapor deposition methods offer conformal coating on textured substrates as well as the possibility for large-scale deposition [19–23]. As highlighted by Abzieher et al., vapor deposition represents a promising pathway toward commercialization, combining scalability, uniformity, and compatibility with industrial requirements [19]. A major drawback is the notoriously difficult control of the volatile organic components, suffering from poor process repeatability [24–29]. Additionally, vapor deposition of organic precursor materials can pose a critical bottleneck for the achievable deposition rates, limiting fabrication throughput [30, 31]. To address these challenges, hybrid two-step deposition routes have emerged, combining conformal vapor deposition of the inorganic precursors with a subsequent solution-based deposition of the organic cations. This method allows for enhanced compositional flexibility, facile introduction of additives and the exclusive usage of green solvents [17, 32–36]. Several studies have extended the knowledge on perovskite film formation using the hybrid two-step deposition route in both SJ [35, 37–41] and tandem configuration, for which PCEs above 31% have been demonstrated on micron-scale textured Si bottom cells [42, 43]. A first study on a large area perovskite/Si TSC reached a promising PCE of close to 28% using blade coating as a scalable solution-based deposition method [44].

A key factor for industrial scalability is the choice of solution deposition technique, with scalable methods such as blade coating, slot-die coating, spray coating, or inkjet printing being of particular interest. Several research groups have demonstrated scalable solution deposition methods for SJ devices [45–49]. While scalable coating techniques are essential, a major challenge for the industrial adaptation of PSCs is the need for high-throughput fabrication. In a previous work by Petry et al. [30], we demonstrated that in case of vapor deposition, the sequential deposition of all precursor materials is desired for high-throughput solar cell fabrication. This approach allows each source to operate at its maximum deposition rate, thereby offering the highest process effectiveness. In contrast, codeposition requires precise control over the relative sublimation rates of multiple materials, complicating process metrology and limiting throughput [30]. So far, most studies using the hybrid two-step deposition route rely on codeposition of the inorganic scaffold, leaving sequential deposition largely unexplored. A thorough comparison of both deposition routes is lacking, which may hinder direct transfer to industrial production.

In this work, we present a fully sequential vapor deposition route of the inorganic scaffold for the hybrid two-step deposition route for wide-bandgap SJ PSCs. We benchmark the sequential deposition route against the conventional codeposition route, demonstrating superior process repeatability and a PCE of 20.3% with a bandgap of 1.70 eV for sequential deposition, ranking among the highest reported PCEs for wide-bandgap hybrid two-step processed SJ PSCs [33–35, 38, 43, 45, 50–62]. Beyond device performance, the sequential deposition route offers clear advantages in simplifying process integration and enhancing scalability, making it a more favorable option for the industrial fabrication of PSCs. Detailed structural analysis reveals distinct differences in the morphology and crystal orientation of the inorganic scaffolds. Further, a strong influence of the elemental distribution depending on the deposition route is indicated, highlighting a pronounced layer structure in the sequentially deposited inorganic scaffold. In summary, our findings underscore the material-level impact of the deposition route already at a fundamental level.

2 | Results and Discussion

The hybrid two-step deposition route encompasses the vapor deposition of the inorganic precursors, followed by a solution-based deposition of the organic precursors. The schematics for both codeposition (Figure 1A, labeled as Co) and sequential deposition (Figure 1B, labeled as Seq) of the inorganic precursor materials PbI_2 and CsCl are illustrated in Figure 1. The incorporation of CsCl into the inorganic scaffold was shown to improve crystallization and enhance the overall quality of the resulting perovskite film [63]. In codeposition, both inorganic precursor materials are sublimated simultaneously. For sequential deposition, CsCl is deposited first, followed by a subsequent deposition of PbI_2.

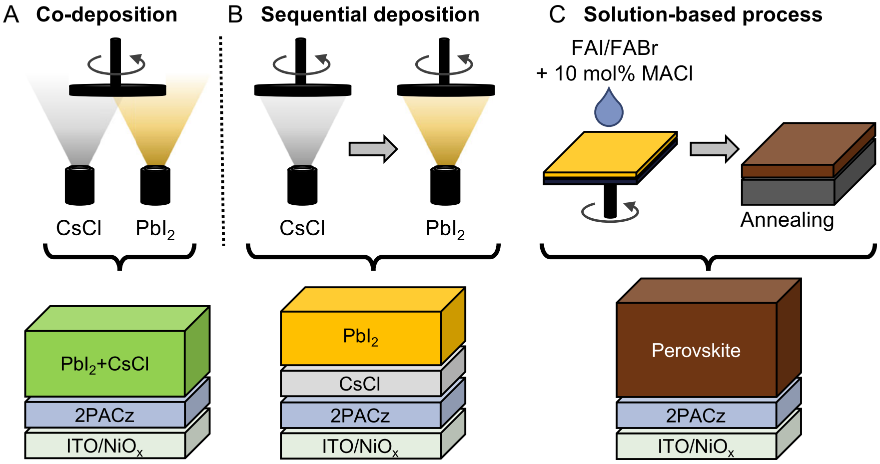

FIGURE 1 | Schematic of the two hybrid two-step deposition routes studied in this work: (A) codeposition (Co) and (B) sequential deposition (Seq) routes of the inorganic precursors CsCl and PbI_2, with the corresponding layer sequence depicted below each process. (C) Schematic illustration of the final perovskite thin film obtained after deposition of the organic cation solution and subsequent thermal annealing under ambient conditions.

Conversion to the final perovskite absorber is realized by depositing the organic cation solution via spin coating, based on an established recipe introduced by Li et al. [33] and Er-raji et al. [35], followed by thermal annealing under ambient conditions (Figure 1C). We adapt a NiO_x/2PACz bilayer as *p*-selective contact, which was found to improve hole extraction and perovskite crystal quality, compared to the reference with only 2PACz [61]. The resulting half-stack devices comprise the layer sequence glass/ITO/NiO_x/2PACz/perovskite. In this study, the perovskite absorber has a nominal composition of $Cs_{0.18}FA_{0.82}Pb(I_{0.76}Br_{0.18}Cl_{0.06})_3$ with a target bandgap of 1.68–1.70 eV (Figure S1). Further details on the fabrication method of the PSCs are described in the Experimental Section.

2.1 | Photovoltaic Performance of PSCs

Despite the fundamentally different process sequences, PSCs fabricated via both codeposition and sequential deposition of the inorganic scaffold exhibit comparable device performance.

To enable a fair comparison of the two deposition routes, conversion of the inorganic scaffold into the perovskite absorber is optimized by varying the molarity of the organic cation solution. Specifically, formamidinium iodide (FAI)/formamidinium bromide (FABr) solutions in the range of 0.65–0.90 M are used with 10 mol% methylammonium chloride (MACl) as an additive.

To assess the repeatability of both deposition routes, six consecutive batches are fabricated for both co- and sequential deposition. For each batch, Figure 2A displays the median PCE, with symbol colors indicating the molarity that yielded the highest PCE within that batch. Two key observations are obtained: First, codeposition shows pronounced batch-to-batch variability, whereas sequential deposition delivers more consistent performance across multiple batches. Second, both deposition routes can achieve comparable device performances. However, the codeposition route exhibits a strong variation in the optimal organic cation solution molarity, which can result in substantially reduced PCE. Consistent with this observation, the optimal organic cation molarity for codeposition is observed to shift between 0.65 and 0.90 M across batches, whereas a narrower optimum of 0.70–0.80 M is retained for the sequential deposition route. A complete overview of the PCE trends for each batch is provided in Figure S2A,B. We note that the final quartz crystal microbalance (QCM) film thicknesses are monitored for each batch, and only minor variations in the measured CsCl QCM thickness are observed for codeposition (30 ± 1 nm), ruling out significant changes in the nominal inorganic scaffold composition (Table S1). The champion device obtained from the sequential deposition route is shown in Figure 2B, for which a maximum PCE of 20.3% is achieved with a V_{OC} of 1.23 V, a J_{SC} of 20.5 mA/cm^2, and a FF of 80.7 % with a bandgap of 1.70 eV (Figure S3B). This device performance ranks among the highest reported PCEs for the hybrid two-step deposition route with a remarkable high V_{OC} approaching 90% of the detailed balance limit (DB limit) for this bandgap (Figure 2C,D with all values given in Table S2), positioning sequential deposition of the inorganic scaffold as a promising deposition route for the fabrication of highly efficient PSCs. Maximum power point (MPP) tracking shows stable device performance for 4000 s (Figure S3C).

In an initial device stability analysis under ISOS-L1 test conditions (100 mW cm^{-2}, 25°C, MPP tracking), the optimal and second-best molarities are examined for codeposition (Figure S4) and sequential deposition (Figure S5). The results in Figure S6 indicate a strong dependence of device stability on organic cation molarity for both deposition routes. Fractional deviations in perovskite stoichiometry are ascribed to influence device stability, highlighting the need for further optimizations and more detailed stability investigations in future studies [64].

Deposition rates of 1 Å s^{-1} for PbI_2 and 0.1 Å s^{-1} for CsCl are selected based on literature reports on codeposition of the

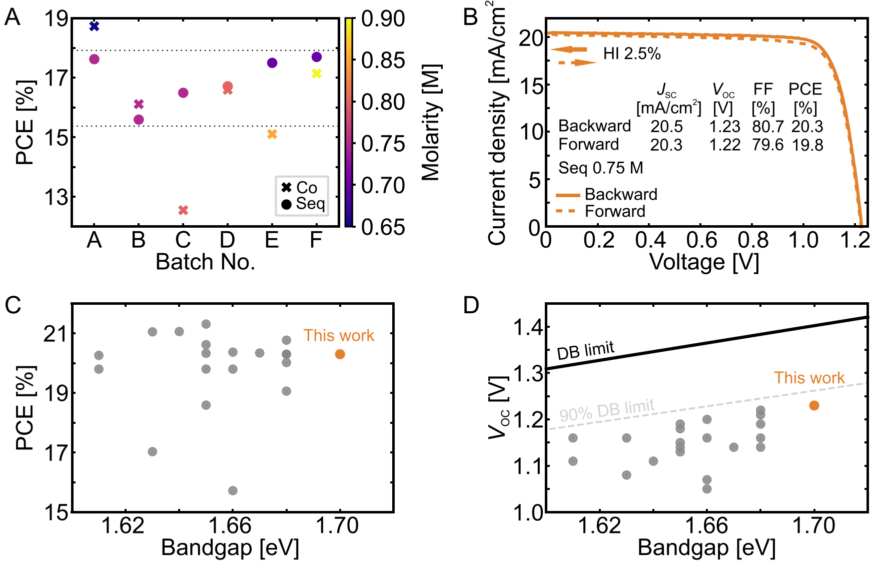

FIGURE 2 | (A) Comparison of process repeatability of PSCs with median PCEs fabricated for co- (Co) and sequential (Seq) deposition of the inorganic scaffold. For each individual batch, Co and Seq PSCs were fabricated in parallel. Symbol colors correspond to the molarity of the organic cation solution resulting in the highest PCE. (B) Champion PSC fabricated with sequential deposited inorganic scaffold with an optimal organic cation molarity of 0.75 M. HI = hysteresis index. (C) PCE versus bandgap and (D) V_{OC} versus bandgap for wide-bandgap (>1.60 eV) hybrid two-step processed PSCs.

inorganic scaffold [33, 35]. These rates are increased using both vertical scale-up (higher rate per source) and horizontal scale-out (multiple sources) strategies [30]. No impact on device performance is observed when the CsCl rate is increased from 0.1 to 0.8 Å s^{-1} (Figure S7) or the PbI_2 rate from 1 to 3 Å s^{-1} (Figure S8). Subsequently, two PbI_2 sources are operated in parallel at 3 + 3 Å s^{-1} to further increase throughput, again yielding comparable device performance (Figure S9). Here, it should be noted that the process window is more prone to shifts, as thickness control is less precise when monitoring two sources simultaneously. Overall, these results demonstrate the compatibility of the sequential inorganic scaffold deposition route with high-throughput PSC fabrication.

As shown in our previous work by Pesch et al. [50], the sequential deposition route is compatible with scalable deposition techniques, such as inkjet printing of the organic cation solution. Using sequential deposition of CsBr and PbI_2 for the inorganic scaffold, SJ PSCs with an efficiency of 19.8% were fabricated. The scalability of the approach was validated on a large-area substrate (6.4 × 6.4 cm^2), yielding a uniform thin film and high PCE homogeneity across the entire substrate. Film homogeneity in our system is primarily governed by source emission characteristics and geometry rather than the deposition route itself [65].

These results highlight an improved process repeatability for the sequential deposition route, both in terms of maximum achievable PCE and a more consistent optimal process window.

All following analysis is conducted with Batch A, also using the respective optimal organic cation solution molarities for the perovskite conversion—0.65 M for codeposition and 0.75 M for sequential deposition—to allow for a fair comparison on a representative cell performance. Detailed photovoltaic performances for Batch A are shown in Figure S10 (Co PSCs) and Figure S11 (Seq PSCs), with the champion PSCs from that batch displayed in Figure S12. Both codeposition and sequential deposition yield a low hysteresis index (HI) below 5%. This minimal hysteresis is considered favorable for *p–i–n* PSCs and indicates reliable device operation. The external quantum efficiency (EQE) spectra and respective optical bandgaps are provided in Figure S1 and the absorptance spectra in Figure S13.

2.2 | Layer Morphology and Microstructure

The morphology and microstructure of the inorganic scaffold exhibit pronounced and systematic differences depending on the deposition route used. These differences are readily apparent upon visual inspection: Codeposition of the inorganic scaffold yields a smooth surface appearance, while sequential deposition produces a distinctly rougher surface (Figure S14). This change in morphology motivates a more detailed investigation using scanning electron microscopy (SEM) and atomic force microscopy (AFM), as shown in Figure 3.

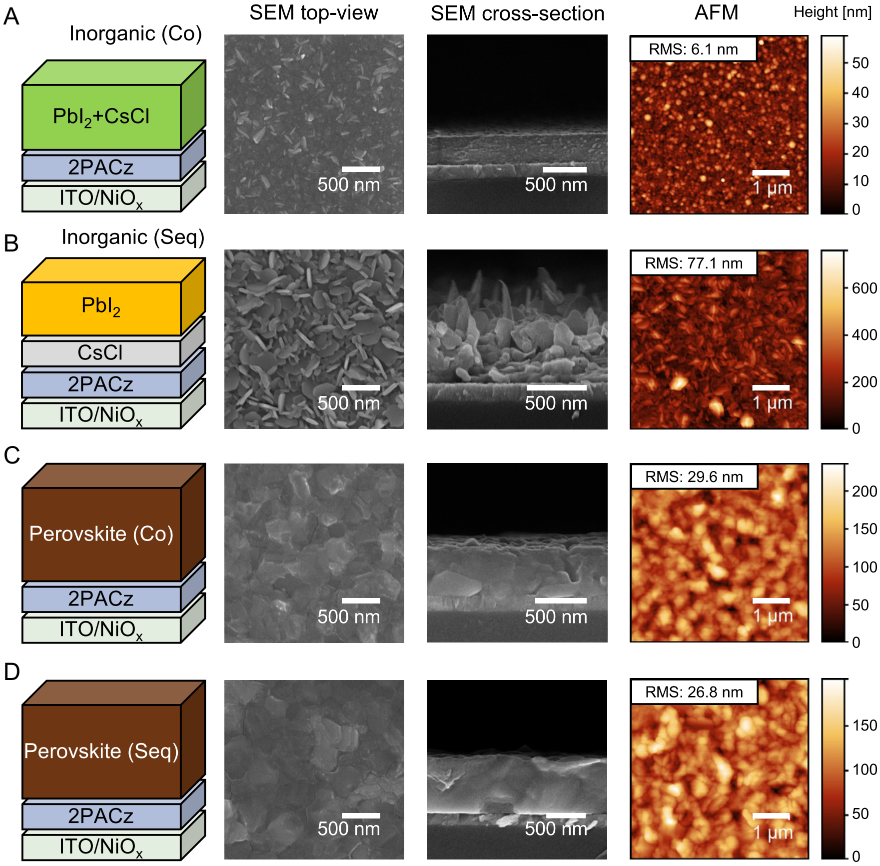

FIGURE 3 | Scanning electron microscopy (SEM) images (top-view and cross-section) and atomic force microscopy (AFM) images of the inorganic scaffold deposited by (A) co- (Co) and (B) sequential (Seq) deposition, as well as of the corresponding perovskite films with (C) co- (Co) and (D) sequential (Seq) deposition of the inorganic scaffold. For the perovskite films, the optimal molarity of the organic cation solution from Batch A is used.

SEM analysis reveals pronounced morphological differences in the inorganic scaffolds (Figure 3A,B), correlating the macroscopic surface appearance with microstructural characteristics. The codeposited inorganic scaffold exhibits a dense, uniform morphology with a smooth surface and a thickness of approximately 330 nm, consistent with QCM measurements and surface profilometry (Figure S15). Individual PbI_2 platelets are not discernible in this case. In contrast, the sequentially deposited inorganic scaffold displays a markedly irregular surface structure, making precise thickness determination challenging. A higher average layer thickness of 409 ± 4 nm is measured with surface profilometry. Sequential deposition of both precursor materials leads to a highly textured microstructure with vertical alignment of PbI_2 platelets, clearly visible in both top-view and cross-section SEM images. Two predominant orientations—either vertical or tilted with respect to the substrate—are apparent.

AFM measurements further support these findings, highlighting a significant difference in surface roughness between the two deposition routes: The codeposited inorganic scaffold exhibits an order of magnitude lower root-mean-square (RMS) surface roughness of 6.1 ± 0.1 nm compared to 77.1 ± 0.4 nm for the sequentially deposited inorganic scaffold. The surface roughness of the inorganic scaffold is an indication of the porosity of the layer, positively impacting the absorption of the organic cation solution into the inorganic scaffold [49]. To assess this, surface structure analysis of a 50 picoliter droplet dispensed on the inorganic scaffold is conducted via confocal scanning microscopy (Figure S16). On the codeposited inorganic scaffold, residual crystalline organic salts accumulate at the center of the dried droplet, indicating limited droplet absorption. In contrast, the sequentially deposited inorganic scaffold shows improved droplet absorption, with less visible organic salt residue remaining.

Despite the very different morphology of the inorganic scaffold, the final perovskite thin films—fabricated by spin coating the optimal molarity of the organic cation solution—exhibit no significant difference in thin-film morphology between both deposition routes (Figure 3C,D). Top-view and cross-section SEM images reveal a comparable microstructure, supported by AFM analysis indicating similar RMS surface roughness values of 29.6 ± 0.7 and 26.8 ± 0.3 nm for codeposition and sequential deposition, respectively. Interestingly, surface profilometry reveals a substantially higher perovskite layer thickness for the sequential deposition route, increasing from 524 ± 4 nm for the codeposition route to 682 ± 5 nm (Figure S15). The expansion coefficients ($\text{thickness}_{\text{perovskite}}/\text{thickness}_{\text{inorganic}}$) for codeposition and sequential deposition are 1.62 and 1.67, respectively, indicating a slightly increased uptake of organic cations in the case of sequentially deposited inorganic scaffolds.

Initial tests of the compatibility of the sequential deposition route with differently textured surfaces are conducted and compared to the codeposition route. To investigate, if the substrate texturing has an impact on layer morphology and microstructure, 550 nm inorganic scaffolds are deposited on planar, nanotextured, and microtextured Si substrates with optical photographies and SEM images of the inorganic scaffolds presented in Figures S17 and S18, respectively. A pronounced change in layer morphology is observed in case of codeposited inorganic scaffolds with a compact inorganic scaffold on planar and a columnar growth on microtextured surfaces. An irregular intermediate inorganic scaffold morphology is observed for nanotextured surfaces. Conversely, in case of sequential deposition, the morphology is independent of the surface texture. Our group has demonstrated that using the sequential deposition route for the inorganic scaffold combined with a scalable deposition technique (inkjet printing) of the organic cation solution enables efficiencies of 27.4% for perovskite/Si TSCs on micron-textured Si bottom cells, underscoring the suitability of this route for tandem integration [50].

In summary, while the deposition route has a substantial impact on the morphology and microstructure of the inorganic scaffold, the morphology of the resulting perovskite absorber layer remains comparable. An initial test of the compatibility of the sequential deposition route with textured surfaces demonstrates texture independent layer morphology.

2.3 | Crystal Orientation

The crystal growth orientation of the inorganic scaffold and consequently the growth behavior of the resulting perovskite absorber are influenced by the deposition route. To further analyze the effect of the deposition route on the microstructural properties of the inorganic scaffold as well as the final perovskite film, grazing-incidence wide-angle X-ray scattering (GIWAXS) measurements are performed (Figure 4). GIWAXS provides insight into the preferred growth direction and overall crystallinity of thin films [66].

Considering the inorganic scaffold, a change in the preferred orientation of the (001) PbI_2 crystal plane is observed from selective growth in the out-of-plane orientation for codeposition to preferred in-plane orientation for sequential deposition as shown in Figure 4A,B. This change in orientation results in a horizontal layer growth of PbI_2 platelets for codeposition and a tendency toward vertical layer growth for sequential deposition, aligning with the observations from SEM analysis (Figure 3). The corresponding distribution of crystallite orientation with integrated intensity over the azimuth angle χ of the (001) PbI_2 crystal plane with a scattering vector of $q = 0.9\ \text{Å}^{-1}$ is shown in Figure 4C. The addition of CsCl in the codeposition route enforces an exclusive horizontal alignment of the (a,b)-plane of PbI_2 relative to the substrate as illustrated in Figure 4D, which is defined as the horizontal mode (I). A similar preferred orientation is found by Meng et al. when depositing pure PbI_2 via a spin-coating route [67]. In contrast, sequential deposition yields a preferred vertical growth, with the (a,b)-plane of PbI_2 vertical relative to the substrate (vertical mode (II), Figure 4D), which appears to be the intrinsic growth mode for pure PbI_2 in vapor deposition processes. We hypothesize that the PbI_2 growth along the (a,b)-plane is thermodynamically preferred, as impinging PbI_2 molecules are bound through ionic forces, whereas the growth along the c-axis is governed by weaker van der Waals forces [68]. Additionally, a secondary preferred growth mode is observed for sequentially deposited inorganic layers with the (a,b)-plane oriented around 40° relative to the substrate (secondary mode (III), Figure 4D). This is consistent with findings by Dierks et al., who compared the surface dependent growth of pure PbI_2 on different hole transport layer (HTL) systems observing a similar secondary orientation at 40° for PTAA, NiO_x, and TaTm [69]. The exact growth mechanism resulting in the surface dependent appearance of the secondary preferred

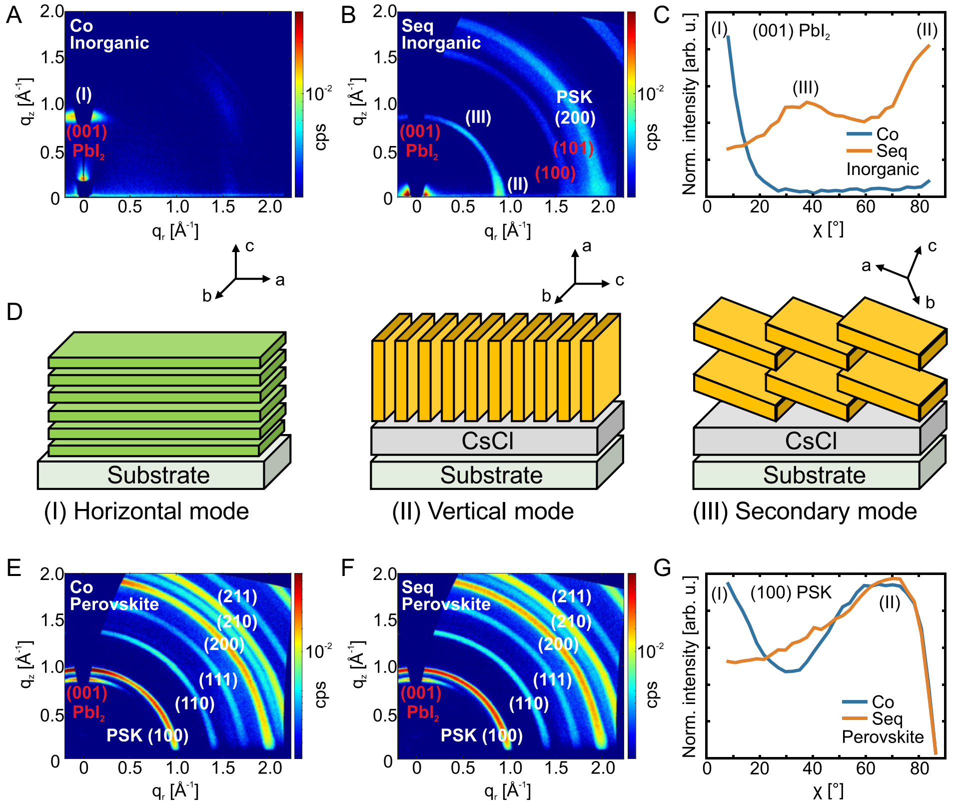

FIGURE 4 | Grazing-incidence wide-angle X-ray scattering (GIWAXS) patterns of the inorganic scaffold deposited by (A) co- (Co) and (B) sequential (Seq) deposition and of the final perovskite films prepared using (E) co- (Co) and (F) sequential (Seq) deposition of the inorganic scaffold. (D) Schematic illustration depicting the orientation of the PbI_2 platelets in the inorganic scaffold for co-deposition (I) and sequential deposition (II)/(III). Distribution of crystallite orientation of the (001) PbI_2 plane in the inorganic scaffolds (C) and (100) perovskite plane in the final perovskite films (G). For the perovskite films, the optimal molarity of the organic cation solution from Batch A is used.

growth direction remains elusive, requiring further investigation, which is beyond the scope of this study.

For the sequentially deposited inorganic scaffold, the GIWAXS signal with scattering vector of $q = 2.0\,\text{Å}^{-1}$ aligns with the expected signal of the (200) perovskite phase and is likewise detected in the corresponding X-ray diffraction (XRD) measurements at 27.6° (Figure S19). This suggests that interfacial reactions between CsCl and PbI_2 may initiate partial perovskite formation. We hypothesize that the concentrations of CsCl and PbI_2 are insufficient in the codeposited inorganic scaffold to initiate the formation of a perovskite phase.

The corresponding perovskite films are also analyzed by GIWAXS measurements, revealing a subtle difference in the preferred crystal orientation of the (100) perovskite phase (Figure 4E–G). Both perovskite films exhibit a discrete Bragg spot around 70°, indicating that it is the intrinsic perovskite growth mode. Interestingly, a secondary small-angle Bragg peak is observed exclusively for the codeposition route (pole figure of the (100) perovskite plane in Figure 4G). We hypothesize that this is due to a templating effect from the horizontally aligned PbI_2 platelets of the inorganic scaffold, which likely undergo topotactic reaction—preserving the crystallographic orientation from the precursor phase [70, 71].

Complementary XRD measurements of the inorganic layers confirm that the crystal orientation is strongly influenced by the deposition route. Specifically, the (001) PbI_2 diffraction peak is more prominent in the codeposited inorganic layer, while the (003) PbI_2 peak is more pronounced in the sequentially deposited inorganic layer (Figure S19). In the resulting perovskite films, similar diffraction peaks with comparable peak intensities and peak area ratios are observed for both deposition routes (Figures S20 and S21). However, the (110) and (111) perovskite peaks appear more pronounced relative to the (100) perovskite peak in perovskite films derived from sequential deposition. For both deposition routes, a small amount of unreacted PbI_2 is observed, consistent with previous studies on two-step processed perovskite films [72, 73]. No diffraction peaks associated with Cs-containing phases are detected, suggesting a complete conversion of CsCl to the final perovskite phase and the absence of secondary phases. Notably, the peak ratio of the (100) perovskite peak to the (001) PbI_2 peak, as well as the full width at half maximum of the (100) perovskite peak, correlates with the molarity of the organic cation solution, highlighting the importance of optimizing the precursor ratio for best device performance (Figures S20 and S21).

In summary, the deposition route has a profound influence on the crystal growth orientation of the inorganic scaffold. These orientation differences are partially preserved during conversion to the perovskite phase, suggesting that the initial alignment of the PbI_2 platelets provides a templating effect during perovskite formation. However, for both deposition routes, comparable PCEs can be achieved, demonstrating that the slight differences in crystal orientation do not severely affect device performance.

2.4 | Elemental Distribution

The deposition route considerably influences the elemental distribution and inter diffusion behavior within the inorganic scaffold and the resulting perovskite absorber layer. To probe the qualitative elemental distribution as a function of depth, a series of time-of-flight secondary ion mass spectrometry (ToF-SIMS) depth profiles are conducted. Characteristic positively charged secondary ions of the relevant species for the inorganic scaffolds and the final perovskite film are displayed in Figure 5A–D, respectively.

Pronounced differences in elemental distribution are observed when comparing the inorganic scaffolds prepared via codeposition (Figure 5A) and sequential deposition (Figure 5B). Ni ($\Sigma(^{58}Ni^+,^{60}Ni^+)$) fragments from the underlying NiO_x HTL are detected in both deposition routes and serve as a positional reference. In the codeposited inorganic scaffold, CsI (CsI^+) and CsCl ($Cs_3Cl_2^+$) fragments accumulate on the top surface and are not homogeneously distributed throughout the inorganic layer. Sequentially deposited inorganic scaffolds show the expected layering with CsCl located exclusively at the HTL interface and PbI_2-containing species ($\Sigma(^{206}PbI^+,^{207}PbI^+,^{208}PbI^+)$) found predominantly at the top surface, consistent with the process order. An additional signal of CsI at the CsCl/PbI_2 interface indicates a spontaneous inter diffusion process of iodide into the CsCl layer. Similarly, PbI_2-containing species accumulate both at the top and bottom of the codeposited inorganic scaffold, possibly due to the relatively high deposition rate of PbI_2, leading to initial substrate coverage.

Counterintuitively, upon conversion to the perovskite layer (Figure 5C,D), Cs ions appear uniformly distributed throughout the layer for both deposition routes, implying a high ionic diffusivity for Cs. The depth profiles of the PbI_2 fragments show similar trends to those observed in the initial inorganic scaffold for both deposition routes. In perovskite layers with codeposited inorganic scaffold, PbI_2 fragments tend to accumulate near the HTL site, whereas in layers with sequentially deposited inorganic scaffold, they are more concentrated at the top surface. Regardless of the deposition route, the organic fragment of FA ($CH_5N_2^+$) is homogeneously distributed throughout the perovskite layer, while MA-related fragments ($\Sigma(CH_4^+,NH_4^+,CH_2N^+,CH_3N^+)$) accumulate primarily at the top surface. This highlights that MACl not only acts as an additive but also incorporates into the perovskite bulk, contrary to previous reports [74–76].

To gain more insights into the distribution and diffusion of the halide components, additional measurements of the negatively charged secondary ions are performed (Figure S22). Distinct differences emerge in the iodide (I^-) and chloride (Cl^-) ion distribution when comparing the inorganic scaffolds. For the codeposited inorganic scaffold, I ions are homogeneously distributed throughout the perovskite film. In contrast, a higher intensity of I ions is measured at the HTL site for the sequentially deposited inorganic scaffold, indicating significant ion diffusion of I into the CsCl layer, effectively forming CsI at the interface. This aligns with the detection of CsI fragments at the interface in the positive ion measurements. Cl ions tend to accumulate at both interfaces for the codeposited inorganic scaffold but only at the bottom interface for sequential deposition, indicating reduced ion diffusion for Cl as compared to I ions. In the final perovskite films, the halide distribution is comparable for both deposition routes. Notably, I ions are homogeneously distributed throughout the layer, while Cl and Br (Br^-) ions show modest accumulation in the center of the perovskite layer.

These findings highlight that the deposition route plays a critical role in shaping the elemental distribution and ion diffusion behavior within both the inorganic scaffold and the resulting

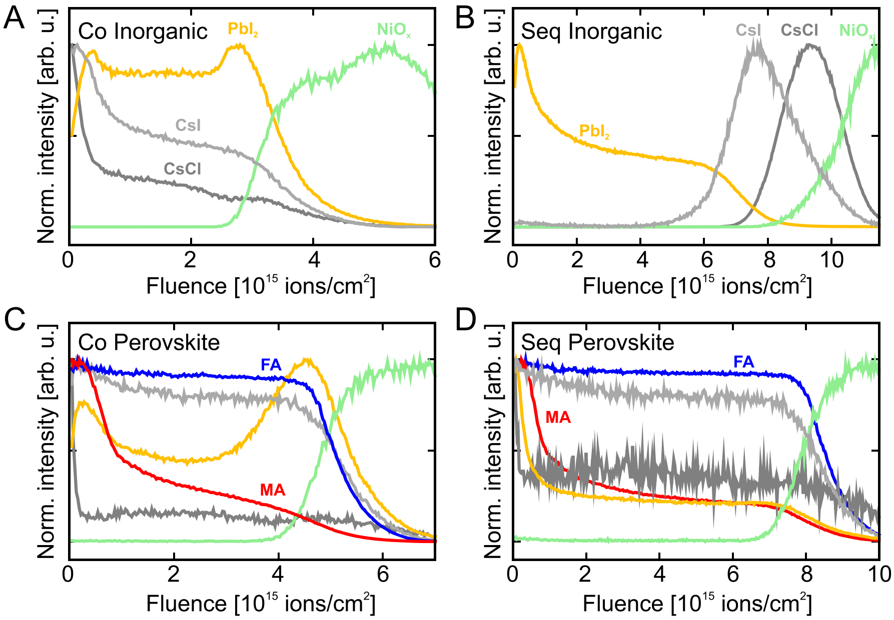

FIGURE 5 | Normed time-of-flight secondary ion mass spectrometry (ToF-SIMS) measurements (positive polarity) of the inorganic scaffold deposited by (A) co- (Co) and (B) sequential (Seq) deposition and of the final perovskite films prepared using (C) co- (Co) and (D) sequential (Seq) deposition of the inorganic scaffold. For the perovskite films, the optimal molarity of the organic cation solution from Batch A is used. The following fragments are displayed: NiO_x, $\Sigma(^{58}Ni^+,^{60}Ni^+)$; PbI_2, $\Sigma(^{206}PbI^+,^{207}PbI^+,^{208}PbI^+)$; CsCl, $Cs_3Cl_2^+$; CsI, CsI^+; FA, $CH_5N_2^+$; and MA, $\Sigma(CH_4^+,NH_4^+,CH_2N^+,CH_3N^+)$.

perovskite absorber. Cs ions exhibit high ion diffusivity, becoming homogeneously distributed regardless of their initial position in the inorganic scaffold. In contrast, Pb components show a lower ion diffusivity and tend to retain their original spatial distribution. The presence of CsI fragments even before thermal treatment implies a high reactivity with spontaneous reaction of the inorganic precursors. Among halide species, a lower diffusion tendency is identified for Cl and Br ions as compared to I ions.

Previous studies have shown that local differences in elemental composition can influence energetic band alignment and, consequently, device performance [77, 78]. However, in the present work, the observed differences in vertical elemental distribution appear to have a minor impact on device performance. While this suggests a limited role of compositional inhomogeneities for the investigated hybrid two-step deposition routes, further targeted investigations are warranted in future work to fully substantiate this conclusion.

3 | Conclusion

This work introduces a fully sequential hybrid two-step deposition route—comprising the sequential deposition of CsCl and PbI_2 for the inorganic scaffold—as a viable alternative to the conventional codeposition route, achieving a PCE of 20.3% for wide-bandgap PSCs and improved process repeatability. Comprehensive analysis reveals distinct differences in the morphology, crystal orientation, and elemental distribution of the inorganic scaffold and perovskite thin film depending on the deposition route. Codeposition results in a horizontal layer growth of PbI_2 platelets (out-of-plane orientation of the (001) plane), whereas sequential deposition promotes vertical growth and a secondary tilted orientation, corresponding to a preferred in-plane crystal orientation of PbI_2. The sequentially deposited inorganic scaffold exhibits an order-of-magnitude increase in surface roughness, reflecting its higher porosity compared to the codeposited counterpart. Elemental distribution analysis reveals a pronounced layer structure for the sequentially deposited inorganic scaffold, indicating a strong dependence on the deposition route. Despite these differences in the inorganic scaffold, the resulting perovskite thin films display comparable surface morphology and only subtle variations in crystal orientation, suggesting that the initial alignment of the PbI_2 platelets plays a templating role during perovskite formation. Elemental distribution analysis indicates high ion diffusivity for Cs, I, and FA ions, which are homogeneously distributed throughout the final perovskite thin film. In contrast, Pb and Cl ions are less diffusive, with spatial distributions largely retained from the initial inorganic scaffold. Overall, this work highlights the influence of the deposition route on the inorganic scaffold in hybrid two-step perovskite fabrication, providing fundamental insights at the material level. As the first study to thoroughly investigate sequential deposition of the inorganic scaffold for PSCs, it lays the groundwork for future research studies aimed at deepening the understanding of the interplay between morphology, crystal growth orientation, and elemental diffusion. Our findings position the sequential deposition route of the inorganic scaffold as a viable route toward industrial PSC production.

4 | Experimental Section

4.1 | Materials

[2-(9H-Carbazol-9-yl)ethyl]phosphonic acid (2PACz: TCI, CAS: 20999-38-6), lead iodide (PbI_2: TCI, 99.99%, trace metals basis, CAS: 10101-63-0), formamidinium iodide (FAI: Greatcell Solar Materials, CAS: 879643-71-7), formamidinium bromide (FABr: Dyenamo, CAS: 146958-06-7), methylammonium chloride (MACl: Dyenamo, CAS: 593-51-1), cesium chloride (CsCl: TCI, ≥99.0% (titration), CAS: 7647-17-8), fullerene-C_{60} (C_{60}: Sigma–Aldrich, CAS: 99685-96-8), bathocuproine (BCP: Lumtec, CAS: 4733-39-5), n-butylammonium iodide (BAI: Greatcell Solar Materials, CAS: 36945-08-1), propane-1,3-diammonium iodide ($PDAI_2$: Greatcell Solar Materials, CAS: 120675-53-8). Ethanol absolute anhydrous, ≥99.8% (EtOH, CAS: 64-17-5), was ordered from VWR Chemicals.

4.2 | Device Fabrication

4.2.1 | SJ PSCs

The planar *p–i–n* PSCs with the layer stack glass/ITO/NiO_x/2PACz/perovskite/$PDAI_2 + BAI/C_{60}$/BCP/Ag were fabricated as follows.

4.2.1.1 | Sample Preparation and Cleaning. The glass substrates with 120-nm-thick indium tin oxide (ITO) coating (sheet resistance $15\,\Omega\,cm^{-2}$, Luminescence Technology, CAS: 50926-11-9) were cut in 16 mm × 16 mm and subsequently cleaned in an ultrasonic bath with acetone and isopropanol for 20 min each. This was followed by 5 min of oxygen plasma treatment before the deposition of the HTL.

4.2.1.2 | Hole Transport Layer. For the HTL, a 5-nm-thick NiO_x film was sputtered from a NiO_x target (4 inch, 99.99% pure, Kurt J. Lesker Company) using 100 W power ($7.95\,W\,in^{-2}$ power density) in a gas mixture of Ar and O_2 at 1 mTorr on the ITO substrate with a fixed flow rate of 0.2 sccm for O_2 and a variable flow rate of Ar to achieve the set pressure. Then, a thin layer of 2PACz was deposited on the ITO/NiO_x substrate by dispensing 75 µL 2PACz solution ($0.5\,mg\,mL^{-1}$ in anhydrous EtOH) on the substrate with a resting time of 5 s followed by rotation at 3000 rpm for 30 s. The substrates were then annealed at a temperature of 100°C for 10 min. A second washing step was used to remove any unbound molecules. Here, 150 µL of pure EtOH was used which was dynamically dispensed onto the substrate within 2 s at 3000 rpm for 30 s of total rotation time. The substrates were then annealed at 100°C for 10 min.

4.2.1.3 | Perovskite Deposition. Vapor deposition of perovskite precursor materials was performed using a PEROvap system (M.Braun Inertgas-Systeme GmbH Dresden) integrated into a nitrogen glovebox. Individual QCMs were used to measure the rate of each material. A cooling inner surface, surrounding all sublimation sources, was set to −20°C. Prior to the heating process, the system was evacuated, with a standard base pressure at start of heating of $<3 \times 10^{-6}$ mbar. For each process, the sublimation rates were kept constant in an automated process. The substrate temperature (18°C) was kept constant for all experiments. Source to substrate setup uses a 300 mm vertical distance and

165 mm lateral distance between the sublimation source and the substrate. Static deposition rates of 1.0 and 0.1 Å s^{-1} of PbI_2 and CsCl, respectively, were used for both sequential and codeposition of the inorganic scaffold. In the case of codeposition, a film thickness of 300 nm was set as the final film thickness for PbI_2, terminating the deposition. The final thickness of CsCl was 30 ± 1 nm for all depositions. For sequential deposition, first 30 nm of CsCl was deposited, followed by 300 nm of PbI_2. For all experiments, cylindrical crucibles with a volume of 10 cm^3 are used with material filling of ≃5 g for PbI_2 and CsCl.

4.2.1.4 | Organic Cation Solution Deposition.

Organic cation solution was deposited via a spin-coating process. A solution of FAI (35%) and FABr (65%) in anhydrous EtOH was prepared with MACl added as an additive with a ratio of 10%mol relative to the total amount of FA^+ [33, 35]. One hundred microliters of the organic cation solution was dispensed dynamically at a rotation speed of 4000 rpm for Batch A and at 5500 rpm for Batches B–F for 30 s. The rotation speed shifted as a result of PeroVap maintenance. The substrates were then annealed at 150°C for 20 min under ambient conditions at a relative humidity of 30%–40%. The spin-coating process took place in a N_2-filled glovebox.

4.2.1.5 | Surface Passivation.

A solution of $PDAI_2$ and BAI was prepared according to Pappenberger et al. by first dissolving 4 mg of $PDAI_2$ under heating in anhydrous EtOH to 50°C [73]. The solution was then transferred to a second vial containing 4 mg of BAI. The solution was agitated using a vortex mixer to yield a stock solution of 1 mg mL^{-1} related to the content of $PDAI_2$. The stock solution was diluted to a concentration of 0.3 mg mL^{-1} with the addition of pure EtOH. For application of the surface passivation, 100 μL of the diluted solution was dispensed on the substrate with a resting time of 5 s followed by rotation at 4500 rpm for 30 s. The substrates were then annealed at 100°C for 5 min.

4.2.1.6 | Electron Transport Layer (ETL) and Top Contact.

As ETL, 20 nm of C_{60} and 5 nm of BCP were thermally sublimed and deposited using an Angstrom evaporation system at an sublimation rate of 0.1–0.2 Å s^{-1} at a pressure of around 10^{-6} mbar. Subsequently, 100 nm Ag was thermally evaporated using a shadow mask to define the active area to 10.5 mm^2 and complete the PSCs with 4 pixels per substrate.

For stability measurements under ISOS-L1 test conditions, semitransparent devices were fabricated. There, BCP was replaced with 20 nm SnO_2 deposited via atomic layer deposition (ALD). The SnO_x layer was deposited using a glovebox-integrated showerhead ALD system (R-200 Advanced, Picosun). The TDMASn source was heated to 70°C, while the TDMASn carrier line was maintained at 125°C during operation. SnO_x films were deposited over 200 ALD cycles. The chamber temperature was set to 90°C. Subsequently, 90 nm indium zinc oxide (IZO) was sputtered from a IZO target (4 inch, In_2O_3/ZnO 90/10 wt%, 99.99% pure, Kurt J. Lesker Company) using 190 W power (15.10 W in^{-2} power density) and a mixture of argon and oxygen (1.3%) at a process pressure of 1.1 mTorr as transparent conductive layer. As top electrode, 75 nm Au was thermally evaporated using a shadow mask to define the active area to 10.5 mm^2 and complete the PSCs with 4 pixels per substrate.

4.3 | Device Characterization

4.3.1 | Current Density–Voltage (J–V) Measurements

The *J–V* characteristics of the SJ PSCs were measured with a class AAA xenon-lamp solar simulator (Newport Oriel Sol3A) with a scan rate set at 0.6 V s^{-1} using a sourcemeter (Keithley 2400) with an air-mass 1.5 global (AM1.5G) spectra (100 mW cm^{-2}, Figure S23). The solar simulator irradiation intensity was calibrated using a certified Si solar cell (Fraunhofer ISE, calibrated 2024) equipped with a KG5 band pass filter (Schott). The device parameters of the light-soaked PSCs were used for the results. The stabilized PCE of the PSCs was determined by measuring the photocurrent at the MPP for 300 s by using a perturb and observing algorithm under continuous AM 1.5G illumination. The measurement was performed in a N_2-filled glovebox. No shadow mask was used for the measurement.

4.3.2 | EQE

The EQE was measured using a PVE300 photovoltaic QE system (Bentham EQE system). A chopping frequency in the range of 560–590 Hz with an integration time of 500 ms was used to acquire the spectra in a wavelength range from 300–850 nm. An illumination spot (0.74 mm) was utilized to obtain the average over possible variations in the EQE spectra. The bandgap of all processed perovskite thin films is determined based on the differential of the EQE curves near the absorption edge (maximum of d(EQE)/d(E)) according to Krückemeier et al. [79].

4.3.3 | SEM

Field emission top-view SEM images were taken with a scanning electron microscope (Zeiss LEO Gemini 1530) with an in-lens detector and an aperture size of 20–30 μm. For cross-sectional analysis, the cross-sections were covered with a 3-nm-thick platinum layer deposited by sputtering to prevent charging. The applied acceleration voltages for surface and cross-sectional analysis range between 5 and 10 kV.

4.3.4 | AFM

AFM images were obtained using a Nano Wizard II (JPK Instruments). The scanning area was 5 μm × 5 μm. For each parameter, 2–3 measurements were conducted, and the average RMS value was determined.

4.3.5 | UV–Vis Spectrophotometry (UV)

Transmittance and reflectance spectra of the perovskite thin films were measured using a PerkinElmer Lambda 1050 spectrophotometry setup equipped with a double-monochromator and a modulated source. A chopper frequency of 46 Hz was applied.

4.3.6 | Confocal Scanning Microscopy

Confocal scanning microscopy measurements were performed with a MarSurf3D system.

4.3.7 | Picoliter Droplet Deposition

Picoliter-sized droplets were dispensed using an optical contact angle and drop contour analyzer (OCA 200, DataPhysics Instruments GmbH) equipped with the picoliter dosing system

(PDDS). Cartridges capable of jetting approximately 50 pL droplets were utilized for this process. The organic cation solution in ethanol with optimal molarity was used in each case.

4.3.8 | XRD

XRD measurements of the inorganic scaffolds and perovskite thin films were performed using a Bruker D2 Phaser system with Cu-K_α radiation ($\lambda = 1.5405$ Å) in Bragg–Brentano configuration using a LynxEye detector. The diffraction pattern was measured for half-stacks with an architecture of glass/ITO/NiO_x/2PACz/perovskite to obtain comparable perovskite nucleation and crystallinity as in the actual device architecture.

4.3.9 | GIWAXS

The GIWAXS measurements were carried out on a Bruker D8 Advance equipped with a Cu X-ray source (40 kV, 40 mA), a Goebel mirror, a 0.5 mm micro mask, and a 0.3 mm snout on the primary track and an Eiger2 R 500K 2D detector on the secondary track. The incidence angle was fixed at 1.5°. First, all acquired images were projected onto a virtual detector directly behind the real goniometer circle using a home-developed program in MATLAB [80]. For reshaping the experimentally acquired data into 2D diffractograms in reciprocal space, the open-access software GIXSGUI was used [81].

4.3.10 | ToF-SIMS

ToF-SIMS was performed on a TOF.SIMS5 instrument (ION-TOF GmbH, Münster, Germany) equipped with a Bi cluster primary ion source and a reflectron type time-of-flight analyzer. UHV base pressure during analysis was $<7 \times 10^{-8}$ mbar. For high mass resolution, the Bi source was operated in the “high current bunched” mode providing short Bi_3^+ primary ion pulses at 25 keV energy, a lateral resolution of approx. 4 µm, and a target current of 0.31–0.35 pA at 10 kHz repetition rate. The short pulse length of 1.5 ns allowed for high mass resolution (6500 m/Δm for $^{208}Pb^+$). The primary ion beam was rastered across a $200 \times 200\ \mu m^2$ field of view on the sample, and 128×128 data points were recorded. Mass scale calibrations were based on Li^+, Na^+, $^{204}Pb^+$, $^{206}Pb^+$, and Cs_2^+ and $^{37}Cl^-$, PO_2^-, CsI_2^-, and PbI_2^-, respectively. For depth profiling, a dual-beam analysis in interlaced mode was performed. For both secondary ion polarities, the sputter gun for depth profiling was operated with Ar_{1500}^+ ions, 10 keV, scanned over a concentric field of $500 \times 500 \mu m^2$ (target current 7.4–7.5 nA). The applied sputter ion fluence was used as an arbitrary measure for depth. Note, however, that this scale might not be linear due to different erosion speeds of the different deposited layers. Secondary ion intensities are plotted normalized to their maximum intensities each, yielding more noise for weaker absolute intensities. It was ensured that signals showing SI detector saturation were omitted.

4.3.11 | Statistical Analysis

PSCs with a V_{OC} below 0.8 V were excluded to filter out statistically irrelevant data. The HI was calculated using HI [%] = [(PCE at backward scan − PCE at forward scan)/PCE at backward scan] · 100.

Acknowledgments

This work was partly carried out with the support of the Karlsruhe Nano Micro Facility (KNMFi) (www.kit.edu/knmf), a Helmholtz Research Infrastructure at Karlsruhe Institute of Technology (KIT) within the project 2024-033-032255. The assistance of Richard Thelen with confocal scanning microscopy measurements within the KMNFi project 2025-033-032285 is acknowledged. Financial support by the Initiating and Networking funding of the Helmholtz Association (Project Zeitenwende and the Solar Technology Acceleration Platform (Solar TAP)), by the Ministry of Science and Culture in the State of Lower Saxony through the program “zukunft.niedersachsen” (project NextGenPV), by the program oriented funding IV of the Helmholtz Association (Materials and Technologies for the Energy Transition, Topic 1: Photovoltaics and Wind Energy, Code: 38.01.04), and the German Federal Ministry for Economic Affairs and Energy (BMWE) through the SHAPE project (03EE1123A-E) is greatly acknowledged. This research was carried out as part of the HyPer project, which is funded by the CETPartnership, under the Joint Call 2023. The CETPartnership’ s research projects are co-funded by the European Commission (Grant Agreement No. 101069750) and the national funding organizations listed on the CETPartnership website. The BMWE funding for the KIT is also listed under the funding code 03EE1222B. We acknowledge support by the Karlsruhe School of Optics & Photonics (KSOP) and the Ministry of Science, Research and Arts of Baden-Württemberg as part of the sustainability financing of the projects of the Excellence Initiative II. This work was partially funded by the European Union. Views and opinions expressed are however those of the author(s) only and do not necessarily reflect those of the European Union or RIA. Neither the European Union nor the granting authority can be held responsible for them. The NEXUS project has received funding from the European Union’s Horizon Europe research and innovation program under grant agreement No. 101075330.

Open Access funding enabled and organized by Projekt DEAL.

Funding

This study was supported by the Helmholtz Association (Project Zeitenwende, Solar Technology Acceleration Platform (Solar TAP), program oriented funding period IV, Materials and Technologies for the Energy Transition, Topic 1: Photovoltaics and Wind Energy, Code: 38.01.04) Niedersächsische Ministerium für Wissenschaft und Kultur (project NextGenPV, “zukunft.niedersachsen”), Bundesministerium für Wirtschaft und Energie (SHAPE project, Grant/Award Number: 03EE1123 A-E, HYPER project, Grant/Award Number: 03EE1222B), Karlsruhe School of Optics & Photonics (KSOP), Ministerium für Wissenschaft, Forschung und Kunst Baden-Württemberg, and European Union (NEXUS, Grant/Award Number: 101075330).

Conflicts of Interest

The authors declare no conflicts of interest.

Data Availability Statement

The data supporting this article has been included as part of the ESI. The data generated during and/or analyzed during the current study has been deposited at the KITopen repository under a CC-BY 4.0 Creative Commons Attribution license: KITopen (2025), https://doi.org/10.35097/0vceqtz3ubr5h240.

References

1. A. Kojima, K. Teshima, Y. Shirai, and T. Miyasaka, “Organometal Halide Perovskites as Visible-Light Sensitizers for Photovoltaic Cells,” *Journal of the American Chemical Society* 131, no. 17 (2009): 6050–6051, https://doi.org/10.1021/ja809598r.

2. National Renewable Energy Laboratory (NREL), “Best Research-Cell Efficiency Chart,” accessed July, 2025, https://www.nrel.gov/pv/cell-efficiency.

3. T. Niewelt, B. Steinhauser, A. Richter, et al., “Reassessment of the Intrinsic Bulk Recombination in Crystalline Silicon,” *Solar Energy Materials and Solar Cells* 235 (2022): 111467, https://doi.org/10.1016/j.solmat.2021.111467.

4. E. Aydin, T. G. Allen, M. D. Bastiani, et al., “Pathways Toward Commercial Perovskite/ Silicon Tandem Photovoltaics,” *Science* 383, no. 6679 (2024): eadh3849, https://doi.org/10.1126/science.adh3849.

5. J. Liu, Y. He, L. Ding, et al., “Perovskite/Silicon Tandem Solar Cells with Bilayer Interface Passivation,” *Nature* 635 (2024): 596–603. https://doi.org/10.1038/s41586-024-07997-7.

6. L. Jia, S. Xia, J. Li, et al., “Efficient Perovskite/Silicon Tandem with Asymmetric Self-Assembly Molecule,” *Nature* 644 (2025): 912–919, https://doi.org/10.1038/s41586-025-09333-z.

7. A. Bhambhani, “*Record 31.1% Efficiency for Trinasolar’s Tandem Solar Cell*,” 2025, https://taiyangnews.info/technology/311-efficiency-perovskite-silicon-tandem-cell-trinasolar.

8. F. Fu, J. Li, T. C.-J. Yang, et al., “Monolithic Perovskite-Silicon Tandem Solar Cells: From the Lab to Fab?”, *Advanced Materials* 34, no. 24 (2022): 2106540, https://doi.org/10.1002/adma.202106540.

9. S. Bächle and A. Kraft, “*Oxford PV and Fraunhofer ISE Develop Full-Sized Tandem PV Module with Record Efficiency of 25 Percent*,” 2024, https://www.ise.fraunhofer.de/en/press-media/press-releases/2024/oxford-pv-and-fraunhofer-ise-develop-full-sized-tandem-pv-module-with-record-efficiency-of-25-percent.html.

10. L. Duan, D. Walter, N. Chang, et al., “Stability Challenges for the Commercialization of Perovskite-Silicon Tandem Solar Cells,” *Nature Reviews Materials* 8, no. 4 (2023): 261–281, https://doi.org/10.1038/s41578-022-00521-1.

11. F. E. Subhan, A. D. Khan, A. D. Khan, et al., “Optical Optimization of Double-Sidetextured Monolithic Perovskite–silicon Tandem Solar Cells for Improved Light Management,” *RSC Advances* 10 (2020): 26631–26638, https://doi.org/10.1039/d0ra04634e.

12. M. De Bastiani, A. J. Mirabelli, Y. Hou, et al., “Efficient Bifacial Monolithic Perovskite/ Silicon Tandem Solar Cells via Bandgap Engineering,” *Nature Energy* 6 (2021): 167–175, https://doi.org/10.1038/s41560-020-00756-8.

13. F. Gota, R. Schmager, A. Farag, and U. W. Paetzold, “Energy Yield Modelling of Textured Perovskite/Silicon Tandem Photovoltaics with Thick Perovskite Top Cells,” *Optics Express* 30 (2022): 14172, https://doi.org/10.1364/oe.447069.

14. W. Qarony, M. I. Hossain, V. Jovanov, et al., “Influence of Perovskite Interface Morphology on the Photon Management in Perovskite/Silicon Tandem Solar Cells,” *ACS Applied Materials & Interfaces* 12 (2020): 15080–15086, https://doi.org/10.1021/acsami.9b21985.

15. A. S. Subbiah, F. H. Isikgor, C. T. Howells, et al., “High-Performance Perovskite Single-Junction and Textured Perovskite/Silicon Tandem Solar Cells via Slot-Die- Coating,” *ACS Energy Letters* 5 (2020): 3034–3040, https://doi.org/10.1021/acsenergylett.0c01297.

16. F. H. Isikgor, F. Furlan, J. Liu, et al., “Concurrent Cationic and Anionic Perovskite Defect Passivation Enables 27.4% Perovskite/ Silicon Tandems with Suppression of Halide Segregation,” *Joule* 5 (2021): 1566–1586, https://doi.org/10.1016/j.joule.2021.05.013.

17. F. Sahli, B. A. Kamino, J. Werner et al., “Fully Textured Monolithic Perovskite/Silicon Tandem Solar Cells with 25.2% Power Conversion Efficiency,” *Nature Materials* 17, no. 9 (2018): 820–826, https://doi.org/10.1038/s41563-018-0115-4.

18. M. Jošt, T. Bertram, D. Koushik, et al., “21.6%-Efficient Monolithic Perovskite/Cu(In, Ga)Se_2 Tandem Solar Cells with Thin Conformal Hole Transport Layers for Integration on Rough Bottom Cell Surfaces,” *ACS Energy Letters* 4, no. 2 (2019): 583–590, https://doi.org/10.1021/acsenergylett.9b00135.

19. T. Abzieher, D. T. Moore, M. Roß, et al., “Vapor Phase Deposition of Perovskite Photovoltaics: Short Track to Commercialization?” *Energy & Environmental Science* 17, no. 5 (2024): 1645–1663, https://doi.org/10.1039/d3ee03273f.

20. Y. Vaynzof, “The Future of Perovskite Photovoltaics–Thermal Evaporation or Solution Processing?,” *Advanced Energy Materials* 10, no. 48 (2020): 2003073, https://doi.org/10.1002/aenm.202003073.

21. L. Gil-Escrig, C. Momblona, M.-G. La-Placa, et al., “Vacuum Deposited Triple- Cation Mixed-Halide Perovskite Solar Cells,” *Advanced Energy Materials* 8, no. 14 (2018): 1703506, https://doi.org/10.1002/aenm.201703506.

22. T. Abzieher, J. A. Schwenzer, S. Moghadamzadeh, et al., “Efficient All-Evaporated *pin* -Perovskite Solar Cells: A Promising Approach Toward Industrial Large-Scale Fabrication,” *IEEE Journal of Photovoltaics* 9, no. 5 (2019): 1249–1257, https://doi.org/10.1109/jphotov.2019.2920727.

23. C. Momblona, O. Malinkiewicz, C. Roldán-Carmona, et al., “Efficient Methylammonium Lead Iodide Perovskite Solar Cells with Active Layers from 300 to 900 nm,” *APL Materials* 2, no. 8 (2014): 081504, https://doi.org/10.1063/1.4890056.

24. L. Cojocaru, K. Wienands, T. W. Kim, et al., “Detailed Investigation of Evaporated Perovskite Absorbers with High Crystal Quality on Different Substrates”, *ACS Applied Materials & Interfaces* 10, no. 31 (2018): 26293–26302, https://doi.org/10.1021/acsami.8b07999.

25. M. Roß, S. Severin, M. B. Stutz, et al., “Co-Evaporated Formamidinium Lead Iodide Based Perovskites with 1000 Hr Constant Stability for Fully Textured Monolithic Perovskite/ Silicon Tandem Solar Cells,” *Advanced Energy Materials* 11, no. 35 (2021): 2101460, https://doi.org/10.1002/aenm.202101460.

26. M. Kroll, S. D. Öz, Z. Zhang, et al., “Insights into the Evaporation Behaviour of FAI: Material Degradation and Consequences for Perovskite Solar Cells”, *Sustainable Energy Fuels* 6, no. 13 (2022): 3230–3239, https://doi.org/10.1039/D2SE00373B.

27. J. Borchert, I. Levchuk, L. C. Snoek, et al., “Impurity Tracking Enables Enhanced Control and Reproducibility of Hybrid Perovskite Vapor Deposition,” *ACS Applied Materials & Interfaces* 11, no. 32 (2019): 28851–28857, https://doi.org/10.1021/acsami.9b07619.

28. I. Levchuk, Y. Hou, M. Gruber, et al., “Deciphering the Role of Impurities in Methylammonium Iodide and Their Impact on the Performance of Perovskite Solar Cells”, *Advanced Materials Interfaces* 3, no. 22 (2016): 1600593, https://doi.org/10.1002/admi.201600593.

29. K. P. S. Zanoni, L. Martínez-Goyeneche, C. Dreessen, M. Sessolo, and H. J. Bolink, “Photovoltaic Devices Using Sublimed Methylammonium Lead Iodide Perovskites: Long-Term Reproducible Processing”, *Solar RRL* 7, no. 7 (2023): 2201073, https://doi.org/10.1002/solr.202201073.

30. J. Petry, V. Škorjanc, A. Diercks, et al., “Industrialization of Perovskite Solar Cell Fabrication: Strategies to Achieve High-Throughput Vapor Deposition Processes,” *EES Solar* 1, no. 3 (2025): 404–418, https://doi.org/10.1039/D5EL00069F.

31. T. Feeney, A. Miaskiewicz, J. Petry, et al., “High-Rate FA-Based Co-Evaporated Perovskites: Understanding Rate Limitations and Practical Considerations to Overcome Their Impact,” *Advanced Functional Materials* (2025): e17873, https://doi.org/10.1002/adfm.202517873

32. P. S. Schulze, K. Wienands, A. J. Bett, et al., “Perovskite Hybrid Evaporation/Spin Coating Method: From Band Gap Tuning to Thin Film Deposition on Textures,” *Thin Solid Films* 704 (2020): 137970, https://doi.org/10.1016/j.tsf.2020.137970.

33. Y. Li, B. Shi, Q. Xu, et al., “Wide Bandgap Interface Layer Induced Stabilized Perovskite/Silicon Tandem Solar Cells with Stability over Ten Thousand Hours,“ *Advanced Energy Materials* 11, no. 48 (2021): 2102046, https://doi.org/10.1002/aenm.202102046.

34. X. Luo, H. Luo, H. Li, et al., "Efficient Perovskite/Silicon Tandem Solar Cells on Industrially Compatible Textured Silicon," *Advanced Materials* 35, no. 9 (2023): 2207883, https://doi.org/10.1002/adma.202207883.

35. O. Er-raji, L. Rustam, B. P. Kore, S. W. Glunz, and P. S. C. Schulze, "Insights into Perovskite Film Formation Using the Hybrid Evaporation/Spin-Coating Route: An In Situ XRD Study," *ACS Applied Energy Materials* 6, no. 11 (2023): 6183–6193, https://doi.org/10.1021/acsaem.3c00698.

36. O. Er-raji, M. A. Mahmoud, O. Fischer, et al., Tailoring Perovskite Crystallization and Interfacial Passivation in Efficient, Fully Textured Perovskite Silicon Tandem Solar Cells," *Joule* 8, no. 10 (2024): 2811–2833, https://doi.org/10.1016/j.joule.2024.06.018.

37. O. Er-raji, C. Messmer, A. J. Bett, et al., "Loss Analysis of Fully-Textured Perovskite Silicon Tandem Solar Cells: Characterization Methods and Simulation toward the Practical Efficiency Potential", *Solar RRL* 7, no. 24 (2023): 2300659, https://doi.org/10.1002/solr.202300659.

38. A. Z. Afshord, B. E. Uzuner, W. Soltanpoor, et al., "Efficient and Stable Inverted Wide-Bandgap Perovskite Solar Cells and Modules Enabled by Hybrid Evaporation- Solution Method," *Advanced Functional Materials* 33, no. 31 (2023): 2301695, https://doi.org/10.1002/adfm.202301695.

39. O. Er-raji, A. J. Bett, S. Lange, et al., "Toward Efficient and Industrially Compatible Fully Textured Perovskite Silicon Tandem Solar Cells: Controlled Process Parameters for Reliable Perovskite Formation", *Progress in Photovoltaics: Research and Applications* 33, no. 1 (2025): 86–99, https://doi.org/10.1002/pip.3770.

40. Q. Xu, B. Shi, Y. Li, et al., "Diffusible Capping Layer Enabled Homogeneous Crystallization and Component Distribution of Hybrid Sequential Deposited Perovskite", *Advanced Materials* 36, no. 5 (2024): 2308692, https://doi.org/10.1002/adma.202308692.

41. A. Ullah, B. Vishal, A. Razzaq, et al., "Improved Crystallinity and Efficiency in Perovskite Solar Cells through Layered Hybrid Deposition," *ACS Energy Letters* 10, no. 1 (2025): 30–33, https://doi.org/10.1021/acsenergylett.4c02797.

42. X. Y. Chin, D. Turkay, J. A. Steele, et al., "Interface Passivation for 31.25% Perovskite/Silicon Tandem Solar Cells," *Science* 381, no. 6653 (2023): 59–63, https://doi.org/10.1126/science.adg0091.

43. Z. Liu, Z. Xiong, S. Yang, et al., Strained Heterojunction Enables High-Performance, Fully Textured Perovskite/Silicon Tandem Solar Cells"," *Joule* 8, no. 10 (2024): 2834–2850, https://doi.org/10.1016/j.joule.2024.06.015.

44. O. Er-raji, A. A. Said, A. S. Subbiah, et al., "Coating Dynamics in Two-Step Hybrid Evaporated/Blade-Coated Perovskites for Scalable Fully-Textured Perovskite/Silicon Tandem Solar Cells," *EES Solar* 1, no. 3 (2025): 419–430, https://doi.org/10.1039/D5EL00073D.

45. X. Zheng, W. Kong, J. Wen, et al., "Solvent Engineering for Scalable Fabrication of Perovskite/Silicon Tandem Solar Cells in Air," *Nature Communications* 15, no. 1 (2024): 4907, https://doi.org/10.1038/s41467-024-49351-5.

46. V. S. Nguyen, I. Zimmermann, E. Grépin, et al., "Solvent-Vapor Assisted Conversion Process for Hybrid Perovskites Coupling Thermal Evaporation and Slot-Die Coating," *Processing Materials Science in Semiconductor* 158 (2023): 107358, https://doi.org/10.1016/j.mssp.2023.107358.

47. X. Yu, X. Yan, J. Xiao, et al., "Interface Modification Effect on the Performance of $CsxFA_{1-x}PbIyBr_{3-y}$ Perovskite Solar Cells Fabricated by Evaporation/Spray-Coating Method," *The Journal of Chemical Physics* 153, no. 1 (2020): 014706, https://doi.org/10.1063/5.0012803.

48. L. Cojocaru, K. Wienands, U. Erdil, et al., "Hybrid Evaporation/Spray-Coating Process for a Simplified and Controllable Production of Perovskite Solar Cells," *IEEE Journal of Photovoltaics* 10, no. 1 (2020): 276–286, https://doi.org/10.1109/jphotov.2019.2949763.

49. R. Pesch, A. Diercks, J. Petry, et al., "Hybrid Two-Step Inkjet-Printed Perovskite Solar Cells," *Solar RRL* 8, no. 13 (2024): 2400165, https://doi.org/10.1002/solr.202400165.

50. R. Pesch, J. Petry, J. Petermann, et al., "Efficient Perovskite/Silicon Tandem Solar Cells Using Hybrid Two-Step Inkjet Printing with Edge Isolation Precision," *Small Science* 5, no. 11 (2025): 2500362, https://doi.org/10.1002/smsc.202500362.

51. J. Chen, S. Yang, L. Jiang, et al., "Surface Molecular Engineering for Fully Textured Perovskite/Silicon Tandem Solar Cells", *Angewandte Chemie International Edition* 63, no. 36 (2024): e202407151, https://doi.org/10.1002/anie.202407151.

52. Y. Li, B. Shi, Q. Xu, et al., "CsCl Induced Efficient Fully-Textured Perovskite/Crystalline Silicon Tandem Solar Cell," *Nano Energy* 122 (2024): 109285, https://doi.org/10.1016/j.nanoen.2024.109285.

53. C. Yang, W. Hu, J. Liu, et al., "Achievements, Challenges, and Future Prospects for Industrialization of Perovskite Solar Cells," *Light: Science & Applications* 13, no. 1 (2024): 227, https://doi.org/10.1038/s41377-024-01461-x.

54. A. A. Said, E. Aydin, E. Ugur, et al., "Sublimed C60 for Efficient and Repeatable Perovskite-Based Solar Cells," *Nature Communications*, 15, no. 1 (2024): 708, https://doi.org/10.1038/s41467-024-44974-0.

55. Z. Xiong, L. Wu, X. Zhou, et al., "Constructing Tin Oxides Interfacial Layer with Gradient Compositions for Efficient Perovskite/Silicon Tandem Solar Cells with Efficiency Exceeding 28%," *Small* 20, no. 15 (2024): 2308024, https://doi.org/10.1002/smll.202308024.

56. T. Yang, L. Mao, J. Shi, et al., "Efficient and Stable Perovskite/Silicon Tandem Solar Cells Modulated with Triple-Functional Passivator", *Advanced Energy Materials* 14, no. 7 (2024): 2303149, https://doi.org/10.1002/aenm.202303149.

57. H. Luo, X. Zheng, W. Kong, et al., "Inorganic Framework Composition Engineering for Scalable Fabrication of Perovskite/Silicon Tandem Solar Cells," *ACS Energy Letters* 8, no. 12 (2023): 4993–5002, https://doi.org/10.1021/acsenergylett.3c02002.

58. Y. Sun, L. Mao, T. Yang, et al., "Ionic Liquid Modified Polymer Intermediate Layer for Improved Charge Extraction toward Efficient and Stable Perovskite/Silicon Tandem Solar Cells," *Small* 20, no. 21 (2024): 2308553, https://doi.org/10.1002/smll.202308553.

59. F. Zhang, B. Tu, S. Yang, et al., "Buried-Interface Engineering of Conformal 2D/3D Perovskite Heterojunction for Efficient Perovskite/Silicon Tandem Solar Cells on Industrially Textured Silicon," *Advanced Materials* 35, no. 42 (2023): 2303139, https://doi.org/10.1002/adma.202303139.

60. O. Er-raji, A. J. Bett, S. Lange, et al., "Toward Efficient and Industrially Compatible Fully Textured Perovskite Silicon Tandem Solar Cells: Controlled Process Parameters for Reliable Perovskite Formation," *Progress in Photovoltaics: Research and Applications* 33, no. 1 (2023): 86–99, https://doi.org/10.1002/pip.3770.

61. L. Mao, T. Yang, H. Zhang, et al., "Fully Textured, Production-Line Compatible Monolithic Perovskite/Silicon Tandem Solar Cells Approaching 29% Efficiency," *Advanced Materials* 34, no. 40 (2022): 2206193, https://doi.org/10.1002/adma.202206193.

62. W. Soltanpoor, C. Dreessen, M. C. Sahiner, et al., "Hybrid Vapor-Solution Sequentially Deposited Mixed-Halide Perovskite Solar Cells," *ACS Applied Energy Materials* 3, no. 9 (2020): 8257–8265, https://doi.org/10.1021/acsaem.0c00686.

63. Q. Luo, M. Wu, H. Zhang, et al., "Combined Evaporation-Solution Methodology for High-Efficiency Perovskite Solar Cells with Exceptional Reproducibility," *Journal of Materials Chemistry A* 13, no. 31 (2025), 25782–25789, https://doi.org/10.1039/d5ta03304g.

64. P. Fassl, V. Lami, A. Bausch, et al., "Fractional Deviations in Precursor Stoichiometry Dictate the Properties, Performance and Stability of Perovskite Photovoltaic Devices," *Energy & Environmental Science*, 11 no. 12 (2018): 3380–3391. https://doi.org/10.1039/c8ee01136b

65. A. Diercks, J. Petry, T. Feeney, et al., “Particle Size Matters – Impact of Particle Size and Crucible Geometry on Sublimation Behavior of Formamidinium Iodide”, *Advanced Materials Technologies* (2025): e01549, https://doi.org/10.1002/admt.202501549.

66. J. A. Steele, E. Solano, D. Hardy, et al., “How to GIWAXS: Grazing Incidence Wide Angle X-Ray Scattering Applied to Metal Halide Perovskite Thin Films,” *Advanced Energy Materials* 13, no. 27 (2023): 2300760, https://doi.org/10.1002/aenm.202300760.

67. K. Meng, X. Wang, Q. Xu, et al., “In Situ Observation of Crystallization Dynamics and Grain Orientation in Sequential Deposition of Metal Halide Perovskites”, *Advanced Functional Materials* 29, no. 35 (2019): 1902319, https://doi.org/10.1002/adfm.201902319.

68. W. Lee, Z. Lyu, Z. Li, P. B. Deotare, and E. Kioupakis, “Spin–Orbit Effects on the Electronic and Optical Properties of Lead Iodide,” *Applied Physics Letters* 122, no. 21 (2023): 212110, https://doi.org/10.1063/5.0146397.

69. A. Diercks, J. Petry, T. Feeney, et al., “Sequential Evaporation of Inverted FAPbI3 Perovskite Solar Cells – Impact of Substrate on Crystallization and Film Formation,” *ACS Energy Letters* 10, no. 3 (2025): 1165–1173, https://doi.org/10.1021/acsenergylett.4c03315.

70. T. M. Brenner, Y. Rakita, Y. Orr, et al., “Conversion of Single Crystalline PbI_2 to CH_3 NH_3 PbI_3: Structural Relations and Transformation Dynamics,” *Chemistry of Materials* 28, no. 18 (2016): 6501–6510, https://doi.org/10.1021/acs.chemmater.6b01747.

71. S. Kumar, V. H. Damle, T. Bendikov, et al., “Topotactic, Vapor-Phase, In Situ Monitored Formation of Ultrathin, Phase-Pure 2D-on-3D Halide Perovskite Surfaces”, *ACS Applied Materials & Interfaces* 15, no. 19 (2023): 23908–23921, https://doi.org/10.1021/acsami.3c01881.

72. R. Pappenberger, A. Diercks, J. Petry, et al., “Bandgap Engineering of Two-Step Processed Perovskite Top Cells for Perovskite-Based Tandem Photovoltaics”, *Advanced Functional Materials* 34, no. 9 (2023): 2311424, https://doi.org/10.1002/adfm.202311424.

73. R. Pappenberger, R. Singh, A. Diercks, et al., “Versatile Two-Step Process for Perovskite- Based Tandem Photovoltaics,” *Solar RRL* 9, no. 13 (2025): 2500193, https://doi.org/10.1002/solr.202500193.

74. M. A. A. Mahmoud, O. Er-Raji, B. P. Kore, et al., “Tuning Perovskite Crystal Growth Dynamics Using Additives on Textured Silicon Substrates,” *Solar RRL* 8, no. 24 (2024): 2400471, https://doi.org/10.1002/solr.202400471.

75. M. M. Tavakoli, M. Saliba, P. Yadav, et al., “Synergistic Crystal and Interface Engineering for Efficient and Stable Perovskite Photovoltaics,” *Advanced Energy Materials* 9, no. 1 (2018): 1802646, https://doi.org/10.1002/aenm.201802646.

76. M. M. Byranvand and M. Saliba, “Defect Passivation of Perovskite Films for Highly Efficient and Stable Solar Cells,” *Solar RRL* 5, no. 8 (2021): 2100295, https://doi.org/10.1002/solr.202100295.

77. Z. Liang, Y. Zhang, H. Xu, et al., “Homogenizing Out-of-Plane Cation Composition in Perovskite Solar Cells,” *Nature* 624, no. 7992 (2023): 557–563, https://doi.org/10.1038/s41586-023-06784-0.

78. S. Li, Y. Jiang, J. Xu, et al., “High-Efficiency and Thermally Stable FACsPbI3 Perovskite Photovoltaics,” *Nature* 635, no. 8037 (2024): 82–88, https://doi.org/10.1038/s41586-024-08103-7.

79. L. Krückemeier, U. Rau, M. Stolterfoht, and T. Kirchartz, “How to Report Record Open-Circuit Voltages in Lead-Halide Perovskite Solar Cells,” *Advanced Energy Materials* 10, no. 1 (2020): 1902573, https://doi.org/10.1002/aenm.201902573.

80. J. C. Fischer, C. Li, S. Hamer, et al., “GIWAXS Characterization of Metal-Organic Framework Thin Films and Heterostructures: Quantifying Structure and Orientation,” *Advanced Materials Interfaces* 10, no. 11 (2023): 2202259, https://doi.org/10.1002/admi.202202259.

81. Z. Jiang, “GIXSGUI: A MATLAB Toolbox for Grazing-Incidence X-Ray Scattering Data Visualization and Reduction, and Indexing of Buried Three-Dimensional Periodic Nanostructured Films,” *Journal of Applied Crystallography* 48, no. 3 (2015): 917–926, https://doi.org/10.1107/s1600576715004434.

Supporting Information

Additional supporting information can be found online in the Supporting Information section. **Supporting Fig. S1:** EQE spectra for different molarities of the organic cation solution for (A) codeposition (Co) and (C) sequential deposition (Seq) of the inorganic scaffold. Optical bandgap extracted from the inflection point of the EQE spectra for (B) codeposition (Co) and (D) sequential deposition (Seq) of the inorganic scaffold from Batch A. **Supporting Fig. S2:** Comparison of process repeatability of PSCs fabricated with co- (Co) and sequential (Seq) deposition of the inorganic scaffold. For each individual batch, Co and Seq PSCs were fabricated in parallel. Each batch comprises 12 pixels per organic cation molarity—for Co and Seq, respectively. The rotation speed for the organic cation solution was increased from 4000 rpm in Batch A to 5500 rpm for Batches B–F to compensate for changed organic cation uptake after PeroVap maintenance. **Supporting Fig. S3:** (A) EQE spectrum as well as the corresponding integrated J_{SC}, (B) optical bandgap extracted from the inflection point of the EQE spectrum, and (C) maximum power point (MPP) tracking for the champion PSC fabricated with sequential deposition of the inorganic scaffold. **Supporting Fig. S4:** Statistical distribution (in total 91 devices) of the open-circuit voltage (V_{OC}), fill factor (FF), short-circuit current density (J_{SC}), and power conversion efficiency (PCE) of semitransparent PSCs for stability measurements under ISOS-L1 test conditions for different molarities of the organic cation solution for codeposition (Co) of the inorganic scaffold. **Supporting Fig. S5:** Statistical distribution (in total 77 devices) of the open-circuit voltage (V_{OC}), fill factor (FF), short-circuit current density (J_{SC}), and power conversion efficiency (PCE) of semitransparent PSCs for stability measurements under ISOS-L1 test conditions for different molarities of the organic cation solution for sequential deposition (Seq) of the inorganic scaffold. **Supporting Fig. S6:** Normalized V_{OC}, J_{SC}, and PCE at the maximum power point (MPP) tracking of semitransparent PSCs with codeposition (Co) and sequential deposition (S_{eq}) of the inorganic scaffold with optimal molarity (best parameter) and second-best parameter under ISOS-L1 test conditions (100 mW cm^{-2}, 25°C, MPP tracking) for 500 h. **Supporting Fig. S7:** Statistical distribution (in total 66 devices) of the open-circuit voltage (V_{OC}), fill factor (FF), short-circuit current density (J_{SC}), and power conversion efficiency (PCE) for increasing deposition rates of CsCl. The molarity of the organic cation solution is 0.77 M and 1 nm of LiF is used as surface passivation. **Supporting Fig. S8:** Statistical distribution (in total 49 devices) of the open-circuit voltage (V_{OC}), fill factor (FF), short-circuit current density (J_{SC}), and power conversion efficiency (PCE) for increasing deposition rates of PbI_2. For this experiment, CsCl was deposited at 0.8 Å s^{-1}. The molarity of the organic cation solution is 0.77 M and 1 nm of LiF is used as surface passivation. **Supporting Fig. S9:** Statistical distribution (in total 70 devices) of the open-circuit voltage (V_{OC}), fill factor (FF), short-circuit current density (J_{SC}), and power conversion efficiency (PCE) for horizontal scale-out of the PbI_2 deposition rate using 3 + 3 Å s^{-1}. ne nanometer of LiF is used as surface passivation. **Supporting Fig. S10:** (A) Statistical distribution (in total 47 devices) of the open-circuit voltage (V_{OC}), fill factor (FF), short-circuit current density (J_{SC}), and power conversion efficiency (PCE), (B) current density versus voltage (J–V) characteristics, and (C) maximum power point (MPP) tracking for different molarities of the organic cation solution for codeposition (Co) of the inorganic scaffold from Batch A. **Supporting Fig. S11:** (A) Statistical distribution (in total 41 devices) of the open-circuit voltage (V_{OC}), fill factor (FF), short-circuit current density (J_{SC}), and power conversion efficiency (PCE), (B) current density versus voltage (J–V) characteristics, and (C) maximum power point (MPP) tracking for different molarities of the organic cation solution for sequential deposition (Seq) of the inorganic scaffold from Batch A. **Supporting Fig. S12:** Current density versus voltage (J–V) characteristics of the champion opaque PSCs with (A) codeposition (Co) and (B) sequential deposition (Seq) of the inorganic scaffold with optimal molarity of the organic cation solution from Batch A. HI = hysteresis index. **Supporting Fig. S13:** Absorptance spectra for the inorganic scaffold as well as the perovskite films with optimal molarity of the organic cation solution fabricated with codeposition (Co) and sequential deposition (Seq) of the inorganic scaffold from Batch A. **Supporting Fig. S14:** Optical photographies of the inorganic scaffolds and the corresponding perovskite films for codeposition (Co) and sequential deposition (Seq). For the perovskite films, the optimal molarity of the organic cation solution from Batch A is used. **Supporting Fig. S15:** Surface profilometry of the inorganic scaffold and corresponding perovskite film with optimal molarity of the organic cation solution for (A) codeposition (Co) and and (B) sequential deposition (Seq) routes from Batch A. The expansion coefficients ($\text{thickness}_{\text{perovskite}}/\text{thickness}_{\text{inorganic}}$) of Co and Seq are 1.62 and 1.67, respectively, indicating a slightly increased organic cation uptake in case of sequentially deposited inorganic scaffolds. **Supporting Fig. S16:** Surface structure analysis via confocal scanning microscopy for (A) codeposition (Co) and (B) sequential deposition (Seq) of the inorganic scaffold. For better visibility, a 10-fold height magnification is chosen for all images. For films with a deposited droplet, the interaction between a single ≈50 pL droplet and the inorganic thin film is examined. For the perovskite films, the optimal molarity of the organic cation solution from Batch A is used. **Supporting Fig. S17:** Optical photographies of the inorganic scaffold deposited by co- and sequential deposition on different textured surfaces ((A/D) planar, (B/E) nanotextured, and (C/F) microtextured). The same HTL stack composed of 15 nm of NiO_x and 2PACz (1 mg/mL) is used and 50 nm CsCl and 500 nm PbI_2 are codeposited or sequentially deposited. **Supporting Fig. S18:** SEM images (cross-section) of the inorganic scaffold deposited by co- and sequential deposition on different textured surfaces ((A/D) planar, (B/E) nanotextured, and (C/F) microtextured). The same HTL stack composed of 15 nm of NiO_x and 2PACz (1 mg/mL) is used and 50 nm CsCl and 500 nm PbI_2 are codeposited or sequentially deposited. **Supporting Fig. S19:** Normed X-ray diffraction (XRD) pattern for (A) the inorganic scaffold and (B) the perovskite film with optimal molarity of the organic cation solution for codeposition (Co) and sequential deposition (Seq) of the inorganic scaffold. ◆ denotes the PbI_2 phase, # the perovskite phase, and ∗ the indium tin oxide (ITO) phase. **Supporting Fig. S20:** Normed X-ray diffraction (XRD) pattern for perovskite films with different molarities of the organic cation solution for (A) codeposition (Co) and (B) sequential deposition (Seq) of the inorganic scaffold. ◆ denotes the PbI_2 phase, # the perovskite phase, and ∗ the indium tin oxide (ITO) phase. Full width at half maximum (FWHM) of the (100) perovskite peak perovskite films with different molarities of the organic cation solution for (C) codeposition (Co) and (D) sequential deposition (Seq) of the inorganic scaffold. **Supporting Fig. S21:** Peak intensity ratios as well as peak area ratios of the X-ray diffraction (XRD) pattern for perovskite films with different molarities of the organic cation solution for (A,C) codeposition (Co) and (B,D) sequential deposition (Seq) of the inorganic scaffold. **Supporting Fig. S22:** Normed time-of-flight secondary ion mass spectrometry (ToF-SIMS) measurements (negative polarity) of the inorganic scaffold deposited by (A) codeposition (Co) and (B) sequential deposition (Seq), as well as of the final perovskite films with (C) codeposition (Co) and (D) sequential deposition (Seq) of the inorganic scaffold. For the perovskite films, the optimal molarity of the organic cation solution from Batch A is used. The following fragments are displayed: NiO_x, NiO_2^-; PO_3, $\Sigma(PO_3^-, PO_3^-)$; PbI_2, $^{267}PbI_3^-$; Cl, Cl^-; I, I^-; Br, Br^-; and CN, CN^-. **Supporting Fig. S23:** Spectrum of the class AAA xenon-lamp solar simulator (Newport Oriel Sol3A) used to measure *J–V* and MPP curves. **Supporting Table S1:** Final quartz crystal microbalance (QCM) thicknesses of CsCl and PbI2 for co- (Co) and sequential (Seq) deposition over multiple batches. **Supporting Table S2:** Literature overview for wide-bandgap PSCs based on hybrid two-step deposition.